JOURNAL OF COMPUTATIONAL PHYSICS 103, 141–159 (1992)

Stability of Explicit Navier–Stokes Procedures Using $k-\varepsilon$ and $k-\varepsilon$/Algebraic Reynolds Stress Turbulence Models

ROBERT F. KUNZ AND BUDUGUR LAKSHMINARAYANA

Department of Aerospace Engineering, Pennsylvania State University, University Park, Pennsylvania, 16802

Received March 4, 1991

A three-dimensional explicit Navier–Stokes procedure has been developed for application to compressible turbulent flows, including rotation effects. In the present work, a numerical stability analysis of the discrete, coupled system of seven governing equations is presented. Order of magnitude arguments are presented for flow and geometric properties typical of internal flows, including turbomachinery applications, to ascertain the relative importance of grid stretching, rotation and turbulence source terms, and effective diffusivity on the stability of the scheme. It is demonstrated through both analysis and corroborative numerical experiments that: (1) It is quite feasible to incorporate, efficiently, a two-equation $k-\varepsilon$ turbulence model in an explicit time marching scheme, provided certain numerical stability constraints are enforced. (2) The role of source terms due to system rotation on the stability of the numerical scheme is not significant when appropriate grids are used and realistic rotor angular velocities are specified. (3) The direct role of source terms in the turbulence transport equations on the stability of the numerical scheme is not significant when appropriate grids are used and realistic freestream turbulence quantities are specified, except in the earliest stages of iteration (a result which is contrary to that generally perceived). (4) There is no advantage to numerically coupling the two-equation model system to the mean flow equation system, in regard to convergence or accuracy. (5) For some flow configurations, including turbomachinery blade rows, it is useful to incorporate the influence of artificial dissipation in the prescription of a local timestep. (6) Explicit implementation of an algebraic Reynolds stress model (ARSM) is intrinsically stable provided that the discrete two-equation transport model which provides the necessary values of k and ε is itself stable.

1. INTRODUCTION

There is ever increasing interest in the numerical solution of the three-dimensional Navier–Stokes equations, since the speed and central memory capacity of digital computers have increased to the point where such calculations can be routinely performed in an engineering environment. As hardware advances have provided the opportunity to model internal and external flows, encountered in aerospace and other applications, a great deal of research has been undertaken to accommodate the complex geometries and flow physics involved.

Throughout the literature, large scale CFD predictions account for the effects of turbulence almost exclusively through the use of eddy viscosity models. Of these, two-equation models have well-documented accuracy advantages over algebraic eddy viscosity models [1]. Nearly as well documented [2] though, are the numerical disadvantages, and thereby the unpopularity, of implementing two-equation models in time-marching Navier–Stokes procedures. The numerical stiffness associated with implicit and explicit computations of the Navier–Stokes and turbulence transport equations on the highly stretched grids required by low-Reynolds number two-equation models has prompted researchers to adopt a variety of strategies to obtain convergent solutions. Wall functions [3–5], for instance, require less near-wall mesh clustering and bridge much of the inner region of the boundary layer, where turbulence source terms are large. Liu [6] has used a hybrid approach, where an algebraic Van Driest damping model is used to model the near-wall physics, thereby also relieving these two stability constraints. Pointwise implicit source term treatment has been used in implicit [2, 7, 8] and explicit [6, 9] codes. Others have cited that particular two-equation models are intrinsically more stable due to their near-wall behavior (i.e., Coakley $q-\omega$ [2, 10], Chien $k-\varepsilon$ [7]). Common to all of these approaches is their success in predicting a variety of complex turbulent flows in convergent fashion. In addition, most of these researchers cite the need for ad hoc stabilization procedures in the early stages of iteration, where source terms can be very large if the flow is initialized in a simple fashion.

Recently, the present authors have successfully computed two- and three-dimensional turbomachinery flowfields using a low-Reynolds number model on very highly stretched grids without alternative near-wall modelling or implicit source term treatment [11, 12]. It was found essential to incorporate mean flow parabolic stability constraints in the specification of a local timestep in configurations where high levels of grid clustering are coincident with

0021-9991/92 $5.00

regions of large effective diffusivities. This is the case in turbomachinery blade row calculations on H- and C-meshes when a two-equation model is used. It was also shown that if appropriate account is taken of these stability constraints, the same CFL numbers can be used as when an algebraic eddy viscosity model is used, and the convergence rates are nearly identical for the two solutions.

The objective of the authors' research is to improve predictions of complex external and internal flows, including turbomachinery flows, through the use of better and practical turbulence models. The current focus of this research is on two-equation and ARSM models. So in lieu of the considerations above, it seemed worthwhile to attempt to provide a more complete analysis of the stability of the discrete system of seven governing equations which arise when a two-equation model is used with the explicit solution procedure. The motivation of such an effort is to reconcile the collective experience of researchers in this area and to quantify the influence of geometric and flow parameters on numerical stability, with emphasis on the turbulence model.

The authors are familiar with two attempts in the literature to analyze the stability of the discrete $k-\varepsilon$ equations. Liu [6], analyzed the 2D "uncoupled" (see terminology discussion below), two-equation $k-\varepsilon$ system and provided an expression for a local timestep based on implicit source term treatment using a two-stage Runge–Kutta procedure. Eliasson [3] provided Von Neumann analysis of the coupled five-equation incompressible 2D Navier–Stokes/$k-\varepsilon$ system. In his work, the influence of turbulence production on the stability of the scheme is neglected. Eliasson thereby obtains that the remaining dissipation terms effectively provide damping to the scheme. He reconciles this result with the observation that it is not necessary to add fourth-order artificial dissipation to the k or ε equations, which has also been the experience of the present authors. Though this neglect of production with respect to dissipation in the stability analysis may be useful when using wall functions, as Eliasson did, it was felt that it would not be appropriate to adopt this simplification in the present work. It is sought here to provide somewhat more general stability results than those obtained by these authors and to perform some numerical verification studies to corroborate the analysis.

First the flow solver and test cases used for the numerical experiments included herein are discussed. The motivation and stability implications of numerically coupling the turbulence transport equations to the mean flow equations are then analyzed and discussed. Next, a vector VonNeumann analysis of the seven discrete, numerically coupled governing equations is undertaken and some local stability results are obtained. Order of magnitude arguments are applied to these results from which some conclusions of relevance to the engineering analyst are drawn. Also, the limitations of the present work and some practical experiences and ad hoc strategies which have been found to be useful are detailed.

2. DESCRIPTION OF FLOW SOLVER AND NUMERICAL TEST CASES

The explicit flow solver used for the numerical studies included herein, is described in detail in Refs. [12, 13]. Briefly, this code is a structured H-grid, explicit, compressible, 3D, full Navier–Stokes flow solver which incorporates a compressible low-Reynolds numer $k-\varepsilon$ model, and includes system rotation and periodic boundaries to accommodate turbomachinery applications. An algebraic Reynolds stress model (ARSM) is available in the code. This model, which incorporates the influence of streamline curvature and system rotation on Reynolds stress anisotropy has been recently modified by the present authors to account for near-wall damping effects. The particular scheme chosen for the numerical experiments undertaken is a standard four-stage Runge–Kutta scheme, first applied to the solution of the Euler equations by Jameson *et al.* [14]. Dissipative operators and source terms are evaluated prior to the first stage. This scheme, whose stability boundary is shown in Fig. 1, was chosen for its familiarity, but the results obtained below are valid for any Runge–Kutta scheme.

In order to provide some verification of the analysis conclusions provided in this paper, a number of parametric studies are undertaken, using this code, applied to a series

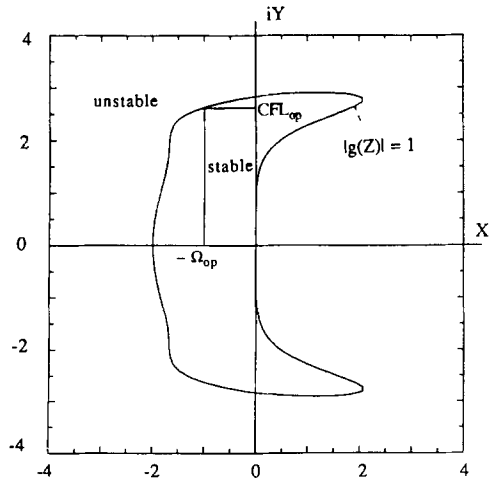

FIG. 1. Stability boundary of Runge–Kutta scheme used for the numerical studies in this paper. The curve represents the contour $|g(Z)| = 1.0$, where Z is the complex fourier symbol, $Z = X + iY$ of a discretized scalar convection–diffusion equation at a particular wavenumber, ang g is the amplification factor arising from a scalar VonNeumann stability analysis of the given scheme applied to this discretized equation.

of numerical test cases. In order to be useful for verification, it is essential to investigate the effect of rotation and turbulence source terms, grid stretching and effective diffusivity, and artificial dissipation. Also, the test cases should typify engineering calculations of complex internal flowfields such as occur in turbomachines. Accordingly, a three-dimensional subsonic compressor rotor and a two-dimensional cascade flow configuration are used. 180,225 and 11,739 point meshes have been used to compute these flows

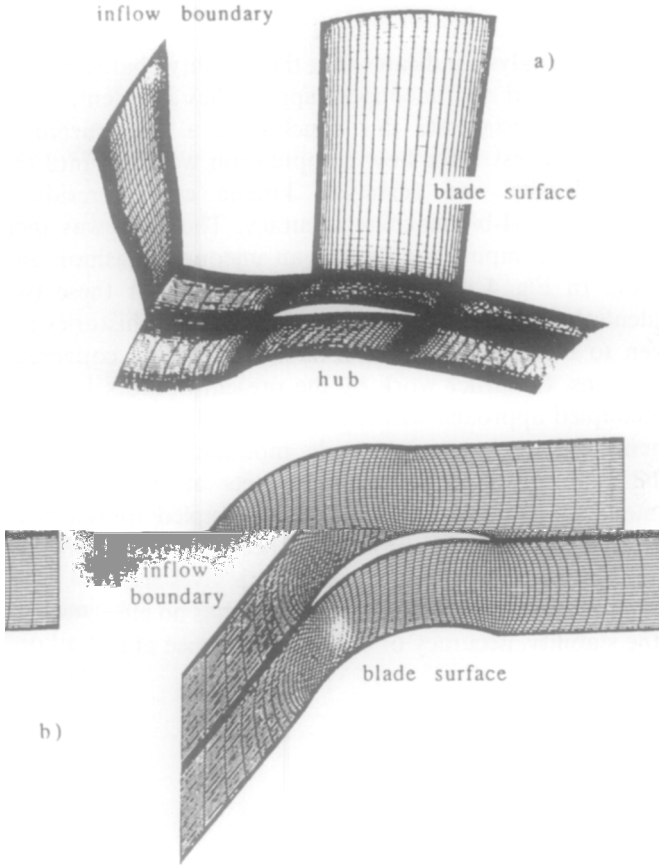

FIG. 2. (a) $89 \times 45 \times 45$ computational mesh used for compressor rotor numerical studies. *Configuration details*: Hub to tip ratio = 0.5, outer annulus wall diameter = 0.936 m, stage has 21 blades; chord length = 0.124 m (hub), 0.154 m (tip); blade stagger angle = 22.5° (hub), 45.0° (tip); flow coefficient, $\Phi = 0.50$; pressure rise coefficient (peak), $\bar{\psi} = 0.55$; rotor shaft angular velocity, $\omega = 113\ s^{-1}$; blade tip speed, $U = 53$ m/s; Reynolds number based on chord length at midspan and rotor tip speed, $R_{cc} = 480{,}000$; ratio of spanwise, axial, and pitchwise grid spacing at midchord and midspan on suction surface = 196:151:1 → $y^+ \cong 6$. (b) 129×91 mesh used for cascade numerical studies. For clarity, only every other grid line is shown in both ξ and η directions. *Configuration details*: Chord length = 0.229 m, space chord ratio = 0.47; blade stagger angle = 20.5°, Reynolds number based on chord length $R_{ec} = 500{,}000$; inlet velocity = 33 m/s at −1.5° incidence; ratio of spanwise to pitchwise grid spacing at midchord on suction surface = 1138:1 → $y^+ < 1$.

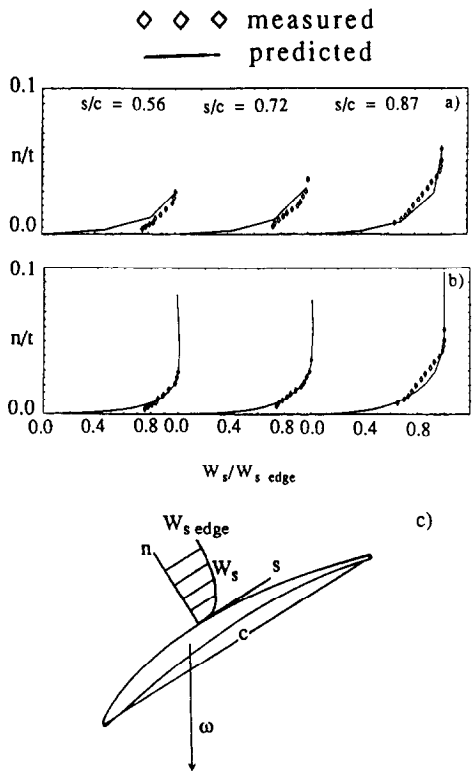

FIG. 3. Comparison of converged rotor midspan streamwise boundary layer velocity profiles using (a) coarse and (b) fine "production run" mesh; (c) nomenclature: s, n = blade tangential and normal coordinates; c, t = chord length, blade spacing; W_s = relative streamwise velocity.

in other work [11, 12], where the code was seen to capture much of the complex viscous flow physics, within the accuracy of the turbulence and tip clearance models used. The computational grids for these cases are shown in Fig. 2, where some properties of the rotor and cascade configurations are also included. The authors feel that these mesh sizes are typical of those used for viscous turbomachinery flow computations in industry. For some of the parametric studies performed herein, it was required to run the code many times. Every fourth grid point was retained from the "production" 3D rotor grid for these cases. The resulting grid, is much too coarse to accurately resolve the near-wall physics, as shown by comparison of the predicted coarse and fine grid midspan boundary layer profiles presented in Fig. 3, but convergence behavior is similar to that of the fine mesh solution.

3. STABILITY ANALYSIS

Uncoupled vs Coupled Turbulence Model

Researchers who have implemented two-equation turbulence models in time-marching Navier–Stokes procedures,

have often adopted schemes where the turbulence transport equations are numerically uncoupled from the mean flow equations [4–7, 9, 11]. In the present context, numerical uncoupling implies that at each iteration the mean flow equations are integrated in time, using frozen values of k and ε (turbulent kinetic energy and dissipation rate, respectively) from the previous iteration. The mean flowfield is then frozen and the turbulence equations are integrated. This procedure is referred to as "uncoupled" by Grasso and Speziale [4], but elsewhere in the literature as "lagged" [7] or "split" [15]. In factored implicit schemes, coupling the two systems of governing equations gives rise to block tridiagonal systems with $(N+2)$ by $(N+2)$ blocks, where N is the number of mean flow equations solved. In explicit multistage schemes, coupling simply implies that fluxes are evaluated at each stage using values of transport variables obtained at the previous stage of the scheme rather than using some values from the previous iteration. The stability of the two approaches is investigated here.

The following development draws on an analysis devised by Lee and Dulikravich [15] to illustrate that their "split" ("uncoupled" in the present context) mean flow-magnetohydrodynamic system solution strategy should not suffer from any stability penalty as compared to the "unsplit" approach.

If dissipation and source terms are evaluated prior to the first stage, the only difference between the coupled and

analyze the nonconservative form of the Euler equations in generalized coordinates,

$$\frac{\partial Q}{\partial t} = -\left[\hat{A}_1 \frac{\partial Q}{\partial \xi} + \hat{A}_2 \frac{\partial Q}{\partial \eta} + \hat{A}_3 \frac{\partial Q}{\partial \zeta}\right], \tag{1}$$

where the transport variable and flux Jacobians are given in Appendix A. If a coupled N-stage Runge–Kutta scheme is applied for temporal discretization of equation 1 we may write

$$Q^{k+1} = Q^0 + \alpha_{k+1}\, \Delta t\, R(Q^k), \qquad k = 0, N-1. \tag{2}$$

A vector VonNeumann stability analysis of Eq. (2) will in general yield an expression for coupled amplification matrix G_c, $Q^N = G_c Q^0$, where G_c is a matrix polynomial function of fourier matrix Z_I, $P(Z_I)$. If an uncoupled Runge–Kutta scheme is applied for temporal discretization of Eq. (1) we may write the uncoupled integration procedure in two steps,

$$\begin{aligned} &\text{(I)} \quad Q^{k+1} = Q^0 + \alpha_{k+1}\, \Delta t\, R_{\text{meanflow}}(Q^k), \quad k = 0, N-1 \\ &\text{(II)} \quad Q^{k+1} = Q^N + \alpha_{k+1-N}\, \Delta t\, R_{k-\varepsilon}(Q^k), \quad k = N, 2N-1, \end{aligned} \tag{3}$$

where the residuals $R_{\text{meanflow}} = R * \text{diag}(1, 1, 1, 1, 1, 0, 0)$ and $R_{k-\varepsilon} = R * \text{diag}(0, 0, 0, 0, 0, 1, 1)$. Each fractional step of the iterative procedure gives rise to an amplification expression, $Q^N = G_{\text{meanflow}} Q^0$ and $Q^{2N} = G_{k-\varepsilon} Q^N$, or for the complete uncoupled procedure $Q^{2N} = G_u Q^0$, where $G_u = G_{\text{meanflow}} G_{k-\varepsilon}$. Here, $G_{\text{meanflow}} = P(\Delta t\, Z_{I\,\text{meanflow}})$, $G_{k\varepsilon} = P(\Delta t\, Z_{Ik-\varepsilon})$, where $Z_{I\,\text{meanflow}} = Z_I * \text{diag}(1, 1, 1, 1, 1, 0, 0)$, $Z_{Ik-\varepsilon} = Z_I * \text{diag}(0, 0, 0, 0, 0, 1, 1)$. Because of the structure of $Z_{I\,\text{meanflow}}$ and $Z_{Ik-\varepsilon}$ we can then say

$$\begin{aligned} G_u &= G_{\text{meanflow}} G_{k-\varepsilon} = P(\Delta t\, Z_{I\,\text{meanflow}})\, P(\Delta t\, Z_{Ik-\varepsilon}) \\ &= P(\Delta t\, Z_{I\,\text{meanflow}} + \Delta t\, Z_{Ik-\varepsilon}) = G_c. \end{aligned} \tag{4}$$

So linear analysis indicates that the stability characteristics of the coupled and uncoupled approaches are identical. In order to substantiate this conclusion, a fully turbulent coarse grid test rotor flow computation was run until the RMS density and turbulent kinetic energy residuals dropped to 64-bit machine accuracy. The code was then retrofit to compute the flow in an uncoupled fashion and rerun. In Fig. 4, the convergence histories for these two calculations are superposed. The convergence histories are seen to be nearly indistinguishable, as are the converged solutions. In earlier work by the present authors [11] an uncoupled approach was chosen to simplify code develop-

timesteps [5] as advantages to an uncoupled approach. In the present work a coupled approach has been adopted. It has been the experience of the authors that this gives rise to a more compact and better organized code and has no affect at all on the stability, accuracy or CPU performance of the scheme.

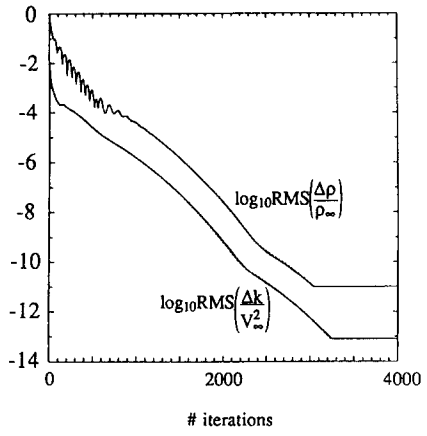

FIG. 4. Comparison of convergence rates for coupled (solid) and uncoupled (dashed) approach.

Vector VonNeumann Procedure

In generalized curvilinear coordinates, the compressible three-dimensional continuity, momentum, energy, turbulent kinetic energy, and turbulent kinetic energy dissipation rate equations can be written in conservation form as

$$\frac{\partial \hat{Q}}{\partial t} = -\left(\frac{\partial \hat{E}}{\partial \xi} + \frac{\partial \hat{F}}{\partial \eta} + \frac{\partial \hat{G}}{\partial \zeta}\right) + \left(\frac{\partial \hat{E}_v}{\partial \xi} + \frac{\partial \hat{F}_v}{\partial \eta} + \frac{\partial \hat{G}_v}{\partial \zeta}\right) + \hat{S}, \qquad (5)$$

where subscript v denotes viscous terms.

The transport variable, flux, and source vectors are given in Appendix A. A compressible form of Chien's [17] low-Reynolds number model is chosen for the analysis. The specific modelling parameters are also included in Appendix A. In the present development, all velocities are relative to a reference frame rotating with constant angular velocity, ω, about the x-axis. The energy variable used is defined as $e_{0R} = e + q^2/2 - \omega^2 r^2/2$, where q represents the magnitude of the relative velocity. A perfect gas equation of state is provided as $p = \rho RT$ (or $p = \rho c^2/\gamma$), where $T = (1/c_v)(e_{0R} - q^2/2 + \omega^2 r^2/2)$. An effective diffusivity formulation has been adopted, where Reynolds (time) averaging is used for pressure and density, and Favre (density-weighted time) averaging is used for velocity components, internal energy, turbulent kinetic energy, and turbulent energy dissipation rate.

We have $\hat{E}_v = \hat{E}_v(\mu_e, Q, Q_\xi, Q_\eta, Q_\zeta)$, $\hat{F}_v = \hat{F}_v(\mu_e, Q, Q_\xi, Q_\eta, Q_\zeta)$, $\hat{G}_v = \hat{G}_v(\mu_e, Q, Q_\xi, Q_\eta, Q_\zeta)$. To simplify the problem, we linearize the viscous flux vectors as $\hat{E}_v = \hat{E}_v(Q_\xi, Q_\eta, Q_\zeta)$, $\hat{F}_v = \hat{F}_v(Q_\xi, Q_\eta, Q_\zeta)$, $\hat{G}_v = \hat{G}_v(Q_\xi, Q_\eta, Q_\zeta)$. So in the stability analysis, we have taken the diffusivities as locally constant, neglected the influence of the components of the normal stress terms, $(\partial/\partial x_i)(-\delta_{ij}\rho k)$, and neglected a heat transfer term proportional to $(\nabla\rho/\rho)\cdot\nabla T$. Such linearizations have also been incorporated in stability analyses performed by other authors [16, 18, 19]. These assumptions are not invoked in the Navier–Stokes procedure but provide simplification in the following analysis. Specifically, they allow us to write the *nonconservative* form of the governing equations, with $Q = (\rho, u, v, w, p, k, \varepsilon)^T$, as

$$\begin{aligned}\frac{\partial Q}{\partial t} = &-\left[\hat{A}_1\frac{\partial Q}{\partial \xi} + \hat{A}_2\frac{\partial Q}{\partial \eta} + \hat{A}_3\frac{\partial Q}{\partial \zeta}\right] + \hat{D}Q \\ &+\left[\hat{S}_1\frac{\partial^2 Q}{\partial \xi^2} + \hat{S}_2\frac{\partial^2 Q}{\partial \eta^2} + \hat{S}_3\frac{\partial^2 Q}{\partial \zeta^2}\right. \\ &\left.+\hat{T}_1\frac{\partial^2 Q}{\partial \xi\,\partial \eta} + \hat{T}_2\frac{\partial^2 Q}{\partial \xi\,\partial \zeta} + \hat{T}_3\frac{\partial^2 Q}{\partial \eta\,\partial \zeta}\right] \qquad (6)\end{aligned}$$

$$\hat{A}_1 = PJ\frac{\partial \hat{E}}{\partial Q}, \quad \hat{A}_2 = PJ\frac{\partial \hat{F}}{\partial Q}, \quad \hat{A}_3 = PJ\frac{\partial \hat{G}}{\partial Q},$$

where

$$\hat{S}_1 = PJ\frac{\partial \hat{E}_v}{\partial Q_\xi}, \quad \hat{S}_2 = PJ\frac{\partial \hat{F}_v}{\partial Q_\eta}, \quad \hat{S}_3 = PJ\frac{\partial \hat{G}_v}{\partial Q_\zeta},$$

$$\hat{T}_1 = PJ\left(\frac{\partial \hat{E}_v}{\partial Q_\eta} + \frac{\partial \hat{F}_v}{\partial Q_\xi}\right), \quad \hat{T}_2 = PJ\left(\frac{\partial \hat{E}_v}{\partial Q_\zeta} + \frac{\partial \hat{G}_v}{\partial Q_\xi}\right),$$

$$\hat{T}_3 = PJ\left(\frac{\partial \hat{F}_v}{\partial Q_\zeta} + \frac{\partial \hat{G}_v}{\partial Q_\eta}\right), \quad \hat{D} = \frac{\partial (PJ\hat{S})}{\partial Q}.$$

These flux and source Jacobians are provided in Appendix A. Matrix P, which scales the viscous and source terms consistent with the operations performed to convert to nonconservative form, also appears there. In the linearization of source Jacobian $\hat{D}$, we take $\hat{S} = \hat{S}(Q)$. Such a linearization has been successfully undertaken in an uncoupled implicit scheme by Sahu and Danberg [7] and in uncoupled explicit schemes which incorporate pointwise implicit treatment of the turbulence equation source terms by Liu [7] and Gerolymos [9]. Additionally, the density is taken as locally constant in linearizing the near wall modelling terms $\mathscr{D}$ and $\mathscr{E}$ (Appendix A). This is justified since these functions are very small except in the immediate vicinity of the wall, where local Mach numbers are low. It is noted that viscous deformation work terms do not appear in the nonconservative form of the energy equation due to our choice of pressure as the dependent variable.

Fourth difference artificial dissipation operators are incorporated in the stability analysis (inclusion of second-order dissipative terms follows analogously and is not included for brevity), so we add to the RHS of Eq. 6,

$$\text{Eq. (6)} + \left[\sigma_\xi I\frac{\partial^4 Q}{\partial \xi^4} + \sigma_\eta I\frac{\partial^4 Q}{\partial \eta^4} + \sigma_\zeta I\frac{\partial^4 Q}{\partial \zeta^4}\right], \qquad (7)$$

where σ_ξ, σ_η, σ_ζ are locally varying dissipation scale factors. These factors are real and negative (so that the fourth difference operators will be dissipative) and have dimension t^{-1}.

If second-order accurate central differences are used to discretize the spatial derivatives, the corresponding Fourier symbols for the spatial derivatives in Eq. (6) and (7) become

$$\begin{aligned} Q_\xi &\to iS_\xi & Q_{2\xi} &\to 2(C_\xi - 1) \\ Q_\eta &\to iS_\eta & Q_{2\eta} &\to 2(C_\eta - 1) \\ Q_\zeta &\to iS_\zeta & Q_{2\zeta} &\to 2(C_\zeta - 1) \\ Q_{\xi\eta} &\to -S_\xi S_\eta & Q_{4\xi} &\to 4(C_\xi - 1)^2 \\ Q_{\xi\zeta} &\to -S_\xi S_\zeta & Q_{4\eta} &\to 4(C_\eta - 1)^2 \\ Q_{\eta\zeta} &\to -S_\eta S_\zeta & Q_{4\zeta} &\to 4(C_\zeta - 1)^2 \end{aligned}$$

where $S_\xi = \sin(\phi)$, $C_\xi = \cos(\phi)$, etc.; ϕ is the phase of the error mode and $\Delta\xi = \Delta\eta = \Delta\zeta \equiv 1$. The fourier symbols given above are consistent with the flux differencing in the code. This is an important consideration as factors of 2 and 4 can appear in the final stability expressions if viscous fluxes are discretized differently.

If a standard multistage Runge–Kutta scheme is incorporated, then a vector VonNeuman stability analysis yields a polynomial expression for the amplification matrix, $G = P(\Delta t\, Z)$, where P represents some matrix polynomial function and Z is the Fourier matrix of the spatial discretization of the governing equations. A necessary condition for stability is spectral radius $\rho(G) \leqslant 1$, for all ϕ. Analyzing the eigenvalues of G for each error mode is not practical computationally. Useful approximations are adopted here to simplify the problem. We split $Z = Z_I + Z_R$, such that $\lambda(Z_I)$ are *all* pure imaginary, and $\lambda(Z_R)$ are *all* pure real, and analyze the individual problems $G_I = P_I(\Delta t\, Z_I)$, $G_R = P_R(\Delta t\, Z_R)$ (where now P_I and P_R need not necessarily be the same polynomial function). Considering the Fourier matrix Z_I (given in Appendix A), we estimate the spectral radius of G_I:

$$\rho(G_I) = \rho(P_I(\Delta t\, Z_I)) \approx P_I(\rho(\Delta t\, Z_I)). \tag{8a}$$

The second equality in Eq. (8a) is strictly true only if $\Delta t\, Z_I$ is hermetian, in which case Eq. (8a) would be a straightforward application of the spectral mapping theorem [21]. In the present context of local linearized analysis, Eq. (8a) is submitted as an approximation which provides useful information, as will be seen.

Matrix Z_R is pure real and there exists an S such that $\bar{Z}_R = S^{-1} Z_R S$ is real and symmetric [18]. That is, the spectral mapping theorem applies directly:

$$\begin{aligned}\rho(G_R) &= \rho(S^{-1} G_R S) = \rho(P_R(\Delta t\, \bar{Z}_R)) \\ &= P_R(\rho(\Delta t\, \bar{Z}_R)) = P_R(\rho(\Delta t\, Z_R)).\end{aligned} \tag{8b}$$

So we have $\rho(G_R) = P_R(\rho(\Delta t\, Z_R))$, and estimate $\rho(G_I) \approx P_I(\rho(\Delta t\, Z_I))$. It remains then only to ensure that the locus of $\rho(\Delta t\, Z_I)$ and $\rho(\Delta t\, Z_R)$ remain simultaneously within the scalar stability boundary for the chosen scheme. Accordingly, if we evaluate all elements of Z_I and Z_R at the phase for which they are a maximum, conservative criteria to ensure stability become

$$\Delta t\, \rho(Z_I) \leqslant i\, CFL_{op} \quad \text{and} \quad \Delta t\, \rho(Z_R) \leqslant \Omega_{op}, \tag{9}$$

where CFL_{op} and Ω_{op} are operational Courant and Von Neumann numbers chosen such that the rectangle formed by, $0 < \Omega < \Omega_{op}$, $0 < CFL < CFL_{op}$ lies within the scalar stability boundary of the chosen scheme (see Fig. 1). Criteria similar to Eq. (9) have been invoked for explicit numerical schemes by other authors [3, 19].

So it is assumed in the above equation that all of the eigenvalues of

$$Z_I = iS_\xi \hat{A}_1 + iS_\eta \hat{A}_2 + iS_\zeta \hat{A}_3 + i(-i\hat{D}_I) \tag{10}$$

are imaginary and that all of the eigenvalues of

$$\begin{aligned}Z_R = {} & 2(C_\xi - 1)\,\hat{S}_1 + 2(C_\eta - 1)\,\hat{S}_2 + 2(C_\zeta - 1)\,\hat{S}_3 \\ & - S_\xi S_\eta \hat{T}_1 - S_\xi S_\zeta \hat{T}_2 - S_\eta S_\zeta \hat{T}_3 \\ & + 4(C_\xi - 1)^2\,\sigma_\xi I + 4(C_\eta - 1)^2\,\sigma_\eta I \\ & + 4(C_\zeta - 1)^2\,\sigma_\zeta I + \hat{D}_R\end{aligned} \tag{11}$$

are real. This assumption will be verified below. Here, for convenience, $\hat{D}$ has been split $\hat{D} = \hat{D}_I + \hat{D}_R$, such that $\lambda(Z_R)$ are all pure real and $\lambda(Z_I)$ are all pure imaginary. $\hat{D}_I$ and $\hat{D}_R$ are given in Appendix A.

Commencing with the hyperbolic analysis, an expression for Z_I (also given in Appendix A) can be obtained from Eq. (10). The seven eigenvalues of Z_I are

$$\begin{gathered}\lambda(Z) = i\bar{U}, \\ i\Big[\bar{U} \pm \tfrac{1}{2}\sqrt{4\omega^2 + 4c\omega k_1 + c^2(k_1^2 + k_2^2 + k_3^2)} \\ \pm \tfrac{1}{2}\sqrt{4\omega^2 - 4c\omega k_1 + c^2(k_1^2 + k_2^2 + k_3^2)}\Big], \\ i\left[\bar{U} \pm \frac{\varepsilon}{k}\sqrt{\left(\frac{P}{\rho\varepsilon} + 1\right)\left(C_1 f_1 \frac{P}{\rho\varepsilon} + C_2 f_2\right)}\right],\end{gathered} \tag{12}$$

where $\bar{U} \equiv US_\xi + VS_\eta + WS_\zeta$ and $k_1 \equiv \xi_x S_\xi + \eta_x S_\eta + \zeta_x S_\zeta$, $k_1 \equiv \xi_y S_\xi + \eta_y S_\eta + \zeta_y S_\zeta$, $k_3 \equiv \xi_z S_\xi + \eta_z S_\eta + \zeta_z S_\zeta$. These eigenvalues are indeed pure imaginary (as per our choice of $\hat{D}_I$), since the groups of terms inside the square root signs are never negative (independent of the sign of ω). The coefficients of the first derivative Jacobians are maximum at $\phi = \pi/2$. A conservative estimate for the maximum value of $\rho(Z_I)$ is therefore obtained by evaluating the trigonometric terms at this phase, so the spectral radius of Z_I,

$$\begin{gathered}\rho(Z_I) \leqslant i\,\mathrm{MAX} \\ \left\{\left[\bar{U} + \frac{1}{2}\sqrt{4\omega^2 + 4c\omega k_1 + c^2(k_1^2 + k_2^2 + k_3^2)}\right.\right. \\ \left. + \frac{1}{2}\sqrt{4\omega^2 - 4c\omega k_1 + c^2(k_1^2 + k_2^2 + k_3^2)}\right], \\ \left.\left[\bar{U} \pm \frac{\varepsilon}{k}\sqrt{\left(\frac{P}{\rho\varepsilon} + 1\right)\left(C_1 f_1 \frac{P}{\rho\varepsilon} + C_2 f_2\right)}\right]\right\},\end{gathered} \tag{13}$$

where now $\bar{U} \equiv |U| + |V| + |W|$, $k_1 \equiv |\xi_x| + |\eta_x| + |\zeta_x|$, $k_2 \equiv |\xi_y| + |\eta_y| + |\zeta_y|$, $k_3 \equiv |\xi_z| + |\eta_z| + |\zeta_z|$. Moving to the parabolic stability analysis, we have:

$$\begin{aligned}\rho(Z_R) = \rho(&2(C_\xi - 1)\,\hat{S}_1 + 2(C_\eta - 1)\,\hat{S}_2 + 2(C_\zeta - 1)\,\hat{S}_3 \\ &- S_\xi S_\eta \hat{T}_1 - S_\xi S_\zeta \hat{T}_2 - S_\eta S_\zeta \hat{T}_3 \\ &+ 4(C_\xi - 1)^2 \sigma_\xi I + 4(C_\eta - 1)^2 \sigma_\eta I \\ &+ 4(C_\zeta - 1)^2 \sigma_\zeta I + \hat{D}_R). \end{aligned} \tag{14}$$

The non-symmetric element of $\hat{S}_i$ does not affect the eigenvalues of $\hat{S}_i$, nor of Z_R; therefore this term can be dropped in the following analysis, so that $\hat{S}_i$ is treated as symmetric and real hereafter. We can invoke the matrix inequality

$$\begin{aligned}\rho(Z_R) \leqslant \|&2(C_\xi - 1)\,\hat{S}_1 + 2(C_\eta - 1)\,\hat{S}_2 + 2(C_\zeta - 1)\,\hat{S}_3 \\ &- S_\xi S_\eta \hat{T}_1 - S_\xi S_\zeta \hat{T}_2 - S_\eta S_\zeta \hat{T}_3 \\ &+ 4(C_\xi - 1)^2 \sigma_\xi I + 4(C_\eta - 1)^2 \sigma_\eta I \\ &+ 4(C_\zeta - 1)^2 \sigma_\zeta I + \hat{D}_R\|, \end{aligned} \tag{15}$$

where $\|\cdot\|$ represents any consistent matrix norm [22]. The triangle inequality provides

$$\begin{aligned}\rho(Z_R) \leqslant &\|2(C_\xi - 1)\,\hat{S}_1\| + \|2(C_\eta - 1)\,\hat{S}_2\| + \|2(C_\zeta - 1)\,\hat{S}_3\| \\ &+ \|-S_\xi S_\eta \hat{T}_1\| + \|-S_\xi S_\zeta \hat{T}_2\| + \|-S_\eta S_\zeta \hat{T}_3\| \\ &+ \|4(C_\xi - 1)^2 \sigma_\xi I\| + \|4(C_\eta - 1)^2 \sigma_\eta I\| \\ &+ \|4(C_\zeta - 1)^2 \sigma_\zeta I\| + \|\hat{D}_R\|. \end{aligned} \tag{16}$$

The coefficients of the second and fourth derivative Jacobians are maximum at $\phi = \pi$ and those of the cross derivative terms are maximum at $\phi = \pi/2$. A conservative estimate for the maximum value of $\rho(Z_R)$ is therefore obtained by evaluating all the trigonometric terms at the phase for which they are the largest:

$$\begin{aligned}\rho(Z_R) \leqslant &4\,\|\hat{S}_1\| + 4\,\|\hat{S}_2\| + 4\,\|\hat{S}_3\| + \|\hat{T}_1\| + \|\hat{T}_2\| + \|\hat{T}_3\| \\ &+ 16\,\|\sigma_\xi I\| + 16\,\|\sigma_\eta I\| + 16\,\|\sigma_\zeta I\| + \|\hat{D}_R\|. \end{aligned} \tag{17}$$

Choosing a matrix 2 norm,

$$\begin{aligned}\rho(Z_R) \leqslant &4[\rho(\hat{S}_1) + \rho(\hat{S}_2) + \rho(\hat{S}_3)] \\ &+ [\rho(\hat{T}_1) + \rho(\hat{T}_2) + \rho(\hat{T}_3)] \\ &+ 16[\rho(\sigma_\xi I) + \rho(\sigma_\eta I) + \rho(\sigma_\zeta I)] + \rho(\hat{D}_R), \end{aligned} \tag{18}$$

where we have used the matrix identity $\|W\|_2 = [\rho(W^T W)]^{1/2}$, and the fact that $\hat{S}_i$, $\hat{T}_i$, $\sigma_i I$, and $\hat{D}_R$ are symmetric and real.

The eigenvalues of $\hat{T}_i$ are complicated, but if it is assumed that the grid is close to orthogonal in regions where the viscous stability bound becomes important (see Martinelli [19]), the eigenvalues of $\hat{T}_1$ are found to be

$$\begin{aligned}&\lambda_1(\hat{T}_1) = \lambda_2(\hat{T}_1) = \lambda_3(\hat{T}_1) = \lambda_4(\hat{T}_1) = \lambda_5(\hat{T}_1) = 0, \\ &\lambda_6(\hat{T}_1) = -\lambda_7(\hat{T}_1) = \frac{\mu_e}{3\rho}\sqrt{(\nabla\xi \cdot \nabla\xi)(\nabla\eta \cdot \nabla\eta)}. \end{aligned} \tag{19}$$

The spectral radius is, therefore

$$\begin{aligned}&[\rho(\hat{T}_1) + \rho(\hat{T}_2) + \rho(\hat{T}_3)] \\ &= \frac{\mu_e}{3\rho}\,[\sqrt{(\nabla\xi \cdot \nabla\xi)(\nabla\eta \cdot \nabla\eta)} \\ &\quad + \sqrt{(\nabla\xi \cdot \nabla\xi)(\nabla\zeta \cdot \nabla\zeta)} + \sqrt{(\nabla\eta \cdot \nabla\eta)(\nabla\zeta \cdot \nabla\zeta)}]. \end{aligned} \tag{20}$$

A simple form for the eigenvalues of $\hat{S}_i$ can be obtained without invocation of a local grid orthogonality assumption, but for consistency with the development for $\hat{T}_i$, such terms are also dropped in $\hat{S}_i$, so that

$$\begin{aligned}&\lambda_1(\hat{S}_1) = 0, \\ &\lambda_2(\hat{S}_1) = \frac{4\mu_e}{3\rho}(\nabla\xi \cdot \nabla\xi), \\ &\lambda_3(\hat{S}_1) = \lambda_4(\hat{S}_1) = \frac{\mu_e}{\rho}(\nabla\xi \cdot \nabla\xi), \\ &\lambda_5(\hat{S}_1) = \frac{\gamma}{\rho}\left(\frac{\mu_l}{\mathrm{Pr}_l} + \frac{\mu_t}{\mathrm{Pr}_t}\right)(\nabla\xi \cdot \nabla\xi), \\ &\lambda_6(\hat{S}_1) = \frac{1}{\rho}\left(\mu_l + \frac{\mu_t}{\mathrm{Pr}_k}\right)(\nabla\xi \cdot \nabla\xi), \\ &\lambda_7(\hat{S}_1) = \frac{1}{\rho}\left(\mu_l + \frac{\mu_t}{\mathrm{Pr}_\varepsilon}\right)(\nabla\xi \cdot \nabla\xi). \end{aligned} \tag{21}$$

For $\gamma = 1.4$, $\mathrm{Pr}_l = 0.72$, $\mathrm{Pr}_t = 0.9$, $\mathrm{Pr}_k = 1.0$, $\mathrm{Pr}_\varepsilon = 1.3$, the spectral radius is therefore,

$$\begin{aligned}&4[\rho(\hat{S}_1) + \rho(\hat{S}_2) + \rho(\hat{S}_3)] \\ &= \frac{4\gamma}{\rho}\left(\frac{\mu_l}{\mathrm{Pr}_l} + \frac{\mu_t}{\mathrm{Pr}_t}\right)(\nabla\xi \cdot \nabla\xi + \nabla\eta \cdot \nabla\eta + \nabla\zeta \cdot \nabla\zeta). \end{aligned} \tag{22}$$

On inspection, $16[\rho(\sigma_\xi I)+\rho(\sigma_\eta I)+\rho(\sigma_\zeta I)] = -16(\sigma_\xi+\sigma_\eta+\sigma_\zeta)$ (recall that the artificial dissipation scale factors are negative and real). Lastly,

$$\lambda(\hat{D}_R) = 0, 0, 0, 0, 0, \frac{2P}{\rho k}-\frac{2\mu_l}{\rho l^2}, \frac{-2C_2 f_2 \varepsilon}{k}-\frac{2\mu_l}{\rho l^2}e^{-y^+/2}. \quad (23)$$

So

$$\rho(\hat{D}_R) = \mathrm{MAX}\left(\left|\frac{2P}{\rho k}-\frac{2\mu_l}{\rho l^2}\right|, \left|\frac{2C_2 f_2 \varepsilon}{k}+\frac{2\mu_l}{\rho l^2}e^{-y^+/2}\right|\right). \quad (24)$$

The spectral radius of Z_R,

$$\begin{aligned}\rho(Z_R) \leqslant \Bigg\{ & \frac{4\gamma}{\rho}\left(\frac{\mu_l}{\mathrm{Pr}_l}+\frac{\mu_t}{\mathrm{Pr}_t}\right)(\nabla\xi\cdot\nabla\xi+\nabla\eta\cdot\nabla\eta+\nabla\zeta\cdot\nabla\zeta) \\ & +\frac{\mu_e}{3\rho}\left[\sqrt{(\nabla\xi\cdot\nabla\xi)(\nabla\eta\cdot\nabla\eta)}\right. \\ & \left.+\sqrt{(\nabla\xi\cdot\nabla\xi)(\nabla\zeta\cdot\nabla\zeta)}+\sqrt{(\nabla\eta\cdot\nabla\eta)(\nabla\zeta\cdot\nabla\zeta)}\right] \\ & -16(\sigma_\xi+\sigma_\eta+\sigma_\zeta) \\ & +\mathrm{MAX}\left(\left[\frac{2P}{\rho k}-\frac{2\mu_l}{\rho l^2}\right|, \left|\frac{2C_2 f_2 \varepsilon}{k}+\frac{2\mu_l}{\rho l^2}e^{-y^+/2}\right|\right)\Bigg\}. \end{aligned} \quad (25)$$

In practice, a stable local timestep could be obtained from

$$\Delta t = \mathrm{MIN}[\Delta t_c, \Delta t_v] \equiv \mathrm{MIN}\left[\frac{CFL_{\mathrm{op}}}{\rho(Z_I)}, \frac{\Omega_{\mathrm{op}}}{\rho(Z_R)}\right], \quad (26)$$

where $\rho(Z_I)$ and $\rho(Z_R)$ are given in Eqs. (13) and (25). It is noted that in the absence of rotation source terms, turbulence model source terms, and artificial dissipation terms, expressions (13) and (25) represent a three-dimensional extension to a form presented by Martinelli [19].

4. ORDER OF MAGNITUDE ANALYSIS

In order to ascertain the relative importance of the various terms which appear in Eqs. (13) and (25), an order of magnitude analysis is undertaken here. It is first observed, upon inspection of Eqs. (13) and (25), that the direct influence of rotation and turbulence source terms can only be *de*stabilizing, for plausible values of ω, k, ε ($-\infty < \omega < \infty$, $k > 0$, $\varepsilon > 0$). For the following arguments, we choose constant reference length scale, l_∞ = blade height and velocity, V_∞ = blade tip speed.

Rotation Source Terms

Upon nondimensionalization, the terms in the square root sign on the second line of Eq. (13) are of order

$$4R_o^2 \pm \frac{4R_o}{M}N_1 + \frac{1}{M^2}(N_1^2+N_2^2+N_3^2), \quad (27)$$

where $R_o = \omega l_\infty / V_\infty$, $M = c/V_\infty$, $N_i = l_\infty/\Delta\bar{x}_i$ are rotation, Mach, and grid clustering parameters. By prescription of the reference scales, V_∞ and l_∞, $O(10^{-1}) < R_o < O(10^0)$. For the compressible flows considered herein, $O(10^{-1}) < M < O(10^0)$. For realistic grids, $O(10^1) < N_i < O(10^5)$. The rotation terms will be most significant when R_o is large, M is large, and N_i is small, that is, in the core flow region. So the third term in Eq. (27) is no less than one order of magnitude greater than the other two terms, which suggests that the rotation terms can be neglected in the specification of a local timestep. To substantiate this conclusion, three fully turbulent coarse grid test rotor flow cases were run. The nondimensional stability parameters, as defined above are $R_o = 0.5$, $M \cong 0.2$, $N_{i\,\min} \cong 10$, for this case. In light of the above arguments, there should be very little influence of the rotation terms in Eq. (13) on the stability of the scheme. In Fig. 5, convergence rates are compared for the cases where ω was set to the machine rotation rate of 113.2 s^{-1} in Eq. (13) and where ω was set to zero in this equation. The plots are indistinguishable, indicating that local timesteps are indeed negligibly influenced by system rotation for this case. Accordingly, the first term in Eq. (13) may be replaced by the more familiar expression:

$$\bar{U} + c(\nabla\xi\cdot\nabla\xi+\nabla\eta\cdot\nabla\eta+\nabla\zeta\cdot\nabla\zeta + 2[\nabla\xi\cdot\nabla\eta+\nabla\xi\cdot\nabla\zeta+\nabla\eta\cdot\nabla\zeta])^{1/2}. \quad (28)$$

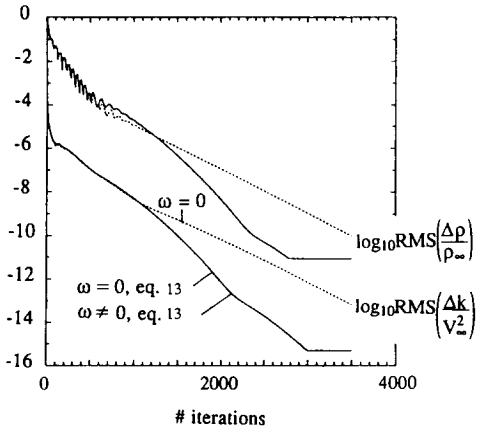

FIG. 5. Comparison of convergence rates for rotating (solid) and stationary (dashed) rotor passage flow with and without inclusion of rotation terms in timestep computations.

The term $\bar{U}$ should be retained as it can be easily shown that this term may be of the same order of magnitude as the other term in Eq. (28) if $M_{\text{local}} = q/c \approx 1$. Also appearing in Fig. 5 is the convergence history for the same case run with

then $(l_\infty/V_\infty)(\varepsilon/k) = O(C_\mu T/C)$, where C is the ratio of integral turbulence length scale to blade height, $L = Cl_\infty$. Reasonable bounds are $O(10^{-3}) < T < O(10^{-2})$, $O(10^{-3}) < C < O(10^{-2})$. So $(l_\infty/V_\infty)(\varepsilon/k) < 10^0$; that is,

are chosen as before. If local turbulence intensity and turbulence length scales are defined,

$$T \equiv \frac{k^{1/2}}{V_\infty}, \qquad L \equiv \frac{C_\mu k^{3/2}}{\varepsilon}, \tag{31}$$

convective acceleration terms in Eq. (13) everywhere in the flowfield. However, the near-wall modelling terms, $2\mu_t/l^2$ and $(2\mu_t/l^2)\, e^{-y^+/2}$ can be very large near solid boundaries and should be considered. Again choosing y as the blade normal coordinate, near solid surfaces the ratio of physical

dissipation to wall correction terms in Eq. (25) is of order $((\mu_l+\mu_t)/\Delta y^2)/(\mu_l/y^2)$. This expression will be very large except in the immediate vicinity of the wall ($\mu_t \to 0$, $y \to \Delta y$), where it approaches unity. So, very near a solid wall, where turbulent diffusivity damping effects dominate, the wall-modelling functions give rise to parabolic stability restrictions that are approximately equal in magnitude to physical diffusion terms. However, it is shown in the next section that convection dominates the overall stability of the scheme in such regions, so it is expected that the wall-modelling terms in Eq. (25) may be neglected as well.

The foregoing arguments suggest neglecting all turbulence source terms in the specification of a local timestep. To investigate this, the relative magnitudes of the terms above were examined for the fine grid rotor and cascade calculations in both early and late stages of iteration. Designating

$$\text{(A)}\quad \frac{\varepsilon}{k}\sqrt{\left(\frac{P}{\rho\varepsilon}+1\right)\left(C_1 f_1 \frac{P}{\rho\varepsilon}+C_2 f_2\right)}$$

$$\text{(B)}\quad \frac{2P}{\rho\varepsilon}\frac{\varepsilon}{k}$$

$$\text{(C)}\quad 2C_2 f_2 \frac{\varepsilon}{k}$$

$$\text{(D)}\quad \frac{2\mu_l}{\rho l^2}$$

$$\text{(E)}\quad \bar{U}+c(\nabla\xi\cdot\nabla\xi+\nabla\eta\cdot\nabla\eta+\nabla\zeta\cdot\nabla\zeta + 2[\nabla\xi\cdot\nabla\eta+\nabla\xi\cdot\nabla\zeta+\nabla\eta\cdot\nabla\zeta])^{1/2}$$

$$\text{(F)}\quad \frac{4\gamma}{\rho}\left(\frac{\mu_l}{\mathrm{Pr}_l}+\frac{\mu_t}{\mathrm{Pr}_t}\right)(\nabla\xi\cdot\nabla\xi+\nabla\eta\cdot\nabla\eta+\nabla\zeta\cdot\nabla\zeta) + \frac{\mu_e}{3\rho}[\sqrt{(\nabla\xi\cdot\nabla\xi)(\nabla\eta\cdot\nabla\eta)} + \sqrt{(\nabla\xi\cdot\nabla\xi)(\nabla\zeta\cdot\nabla\zeta)} + \sqrt{(\nabla\eta\cdot\nabla\eta)(\nabla\zeta\cdot\nabla\zeta)}].$$

For the fine grid rotor flow computation, at convergence, the magnitudes of terms A, B, and C were less than 0.1 times the magnitude of term E, and the magnitude of term D was less than 0.1 times the magnitude of term F, at every point in the computational domain, thereby substantiating the arguments of the previous section for this case. Upon cold start "inviscid" initialization the same conditions were observed except for term B. Specifically, at iteration 1, the magnitude of term B was greater than one-tenth the value of term E at approximately 0.15 of the grid points in the flowfield. This number decreased to 0.002 in 250 iterations. For the cascade computation, the ratio of these terms were all less than 0.1, both at iteration 1 and at convergence.

Some discussion is warranted here. The foregoing arguments suggest that the stiffness associated with large values of near wall turbulence transport source terms is negligible for Chien's model, except in early stages of iteration. Rather, the well-known stiffness (local timestep restriction) associated with computing flows on very highly stretched grids, using time marching algorithms supersedes difficulties brought about by these source terms. For this reason, the present authors have been able to successfully compute a variety of high Reynolds number flowfields using this model [11–13], without taking account of the $k-\varepsilon$ source terms in the determination of a local timestep and with evaluation of source terms prior to the first stage only. Additionally, the convergence rates have been shown to be nearly identical to calculations performed using an algebraic eddy viscosity model [11].

Since the source terms do not significantly influence the stability the scheme, the use of locally implicit treatment of the source terms should not be necessary. This reconciles with recent results obtained by Martelli and Michelassi [8] who used a factored implicit time marching scheme. They found that pointwise implicit treatment for the source terms in the near-wall $q-\omega$ model they used provided no difference in the convergence rate over a purely explicit treatment. This relative insensitivity of scheme stability to source term treatment has apparently also been the experience of other authors using explicit time marching procedures and low Reynolds number turbulence models [25, 28].

To investigate this further, the fine grid cascade computation was run three times. First the standard approach was used, where all source and dissipative terms are evaluated prior to the first stage. Next, the code was run evaluating all source and dissipative terms at every stage. Last, the code was run using pointwise implicit treatment of the *turbulence* source terms. Specifically, for the k and ε equations, each stage in the standard RK4 procedure (Eq. (2)) is replaced by

$$Q^{k+1} = Q^0 + \alpha_{k+1}\,\Delta t[I-\alpha_{k+1}\,\Delta t\hat{D}^k]^{-1}R(Q^k), \qquad k=0,N-1, \tag{34}$$

where $\hat{D}$ is given in Appendix A. For each of the three computations, $\mathrm{CFL}_{\mathrm{op}}$ was chosen as 2.8, and Ω_{op} was adjusted to the maximum value for which a stable solution could be obtained. Specifically, $\Omega_{\mathrm{op1}}=0.95$, $\Omega_{\mathrm{op2}}=0.80$, $\Omega_{\mathrm{op3}}=0.80$. The convergence histories for these calculations appear in Fig. 6a. In Fig. 6b, the predicted boundary layer velocity and turbulent kinetic energy profiles at $s/c=0.2$ on the suction surface are compared. The convergence histories are quite similar for all three approaches, and the converged solutions are indistinguishable. These findings further substantiate the claims made above.

Recently, Gerolymos [9] obtained two-dimensional supersonic duct flow results on very fine meshes, using an

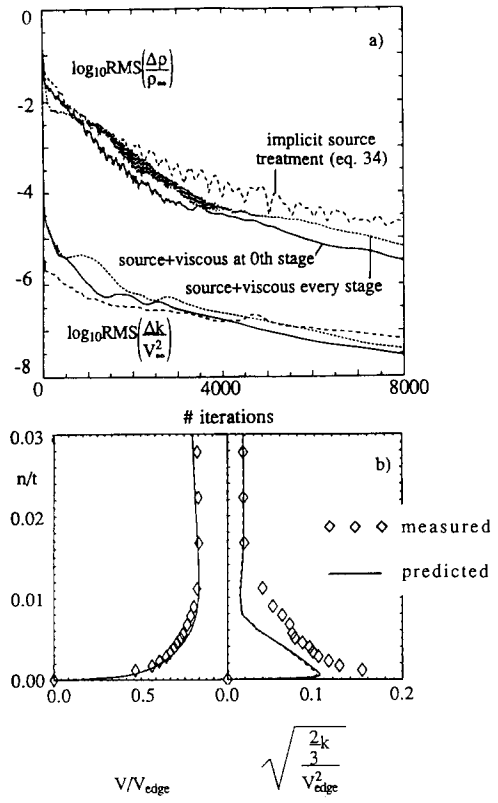

FIG. 6. Comparison of (a) convergence histories, (b) converged boundary layer velocity and local turbulence intensity profiles at a location on the suction surface for fine grid cascade computations. Results for three different source and dissipation term treatments are compared.

explicit multigrid scheme and a low Reynolds number model due to Launder and Sharma [29]. This model is similar to Chien's in that the isotropic component of dissipation is a transport variable. Gerolymos notes that "for both the driver scheme and the multiple-grid procedure, [pointwise implicit treatment] of the source terms is essential to the stability of the method." Since the source term linearization he chose is the same as analyzed and used above, his statement for the driver scheme is in some contradiction to the present findings. However, when a multigrid procedure is incorporated, the conclusions reached above become less valid if the complete residuals, including source terms, are evaluated on successively coarser grids. Specifically, grid metric stability constraints associated with convection and diffusion operators are relaxed when going to coarser grids, whereas timestep constraints associated with the source terms are not. This is pointed out by Mavriplis and Martinelli [33], who, like Gerolymos, chose a multigrid procedure, where the turbulence source term residuals are retained on coarse grids. They justify using implicit source treatment so that these source terms will not limit the larger timesteps allowed by relaxing the convection and diffusion stability constraints on coarser grids.

In practice the authors have encountered several cases, including flat plate and supersonic cascade flow computations, where large relative values of production, $P/\rho\varepsilon$, cause the turbulence model to become rapidly unstable in the early stages of iteration. These cases have in common that freestream turbulence levels are low and Reynolds numbers are high. We have found that incorporation of the turbulence source terms in Eqs. (13) and (25) is *ineffective* in stabilizing these cases. However, several procedures are effective. Specifically, k and ε are required to remain positive

$$\rho\varepsilon > K_\varepsilon \rho_\infty \varepsilon_\infty \tag{35a}$$

$$\rho k > K_k \rho_\infty k_\infty, \tag{35b}$$

where $K_\varepsilon = 0.01 - 0.0001$ and $K_k = 0.0001$. This procedure was recommended to the authors by Connell [28] and is used by Gerolymos [9]. Also the inflow turbulence intensity can be increased to an unrealistically high value for the first 20–50 iterations,

$$T_\infty = 5T_{\infty\,\text{actual}}. \tag{35c}$$

This has the effect of significantly reducing $P/\rho\varepsilon$ in the early stages of iteration, since upon initialization, $P/\rho\varepsilon = O(\mu_t/\varepsilon) = O(1/T_\infty^2)$. Incorporation of these three procedures has allowed us to compute all of the flow configurations we have attempted with the code in a convergent fashion. Accordingly, rotation and turbulence source terms are not included in the specification of a local timestep, in either the computations to follow, or in practice.

Physical and Artificial Dissipation

The physical diffusion terms in Eq. (25) are both of order

$$\left(\frac{1}{R_{el}} + \frac{1}{R_{et}}\right) N_i^2, \quad \text{where} \quad R_{el} \equiv \frac{\rho V_\infty l_\infty}{\mu_l}, \quad R_{et} \equiv \frac{\rho V_\infty l_\infty}{\mu_t}. \tag{36}$$

In many internal and external flows including turbomachinery flows, we have $R_{el} \approx O(10^5 - 10^6)$ and $(10^1) < R_{et} < O(10^5)$, except in regions where wall damping is effective (where $R_{et} \to \infty$). So comparing the inviscid terms in Eq. (28), which are of order $(1/M)N_i$, we invoke the bounds on M and N_i that are provided in the previous sections and conclude that the parabolic timestep may be smaller than the hyperbolic term, $\Delta t_v < \Delta t_c$, in regions of very high grid clustering ($N_i = O(10^5)$) and low R_{et} ($= O(10^1)$), i.e., $(1/R_{et})N_i^2 > (1/M)N_i$. In Fig. 7, the $\Delta t_v/\Delta t_c = 1$ contour is plotted for the fully converged coarse grid and production rotor computations at an annular grid slice near midspan. In both cases, the parabolic stability

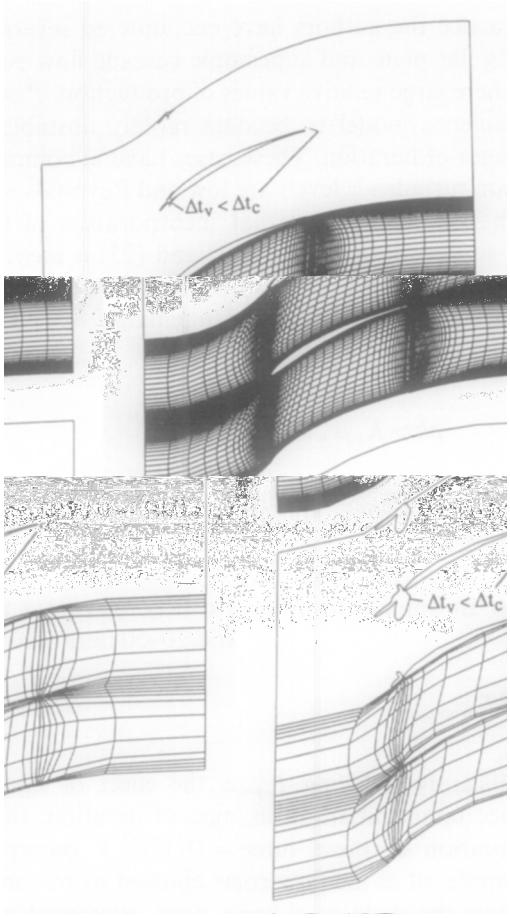

FIG. 7. Regions of computational domain where $\Delta t_v < \Delta t_c$ for (a) fine grid and (b) coarse grid rotor flow calculations at convergence (annular grid slice near midspan).

considerations described above are seen to manifest themselves near the leading and trailing edges. This provides numerical verification of the necessity to include the effective diffusivity terms in Eq. (25), in calculations where large diffusivities occur in regions of large grid stretching. It has been the experience of the authors, that this is especially important during the course of iteration as illustrated in Fig. 8. There it is shown that the parabolic stability bound dominates for more than half of the mesh points in early stages of iteration for the coarse grid test flow configuration, and for 7% of the mesh points at convergence. The cascade computation yielded similar results. Specifically, at convergence $\Delta t_v < \Delta t_c$ for 4% of the mesh points, all in the immediate vicinity of the blade leading and trailing edges.

Artificial dissipation is added to the discrete equations, by design, to influence the stability of the scheme. If physical dissipation gives rise to a locally dominant parabolic stability constraint, any artificial dissipation will destabilize the calculation. Therefore, the artificial dissipation terms in Eq. (25) must be retained if maximum operational Von Neumann numbers are to be used independent of levels of added dissipation. This is illustrated in Fig. 9. The solid line

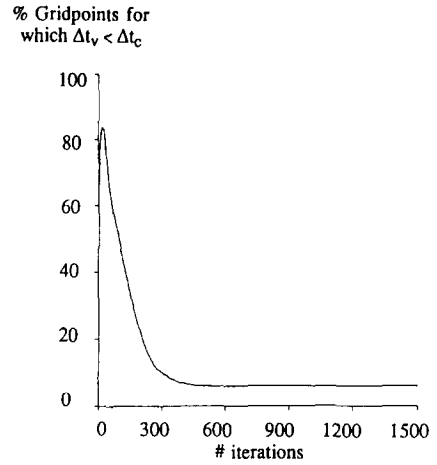

FIG. 8. Percentage of mesh points for which $\Delta t_v < \Delta t_c$ as a function of iteration number for coarse grid rotor flow computation.

in this figure is the convergence history for the coarse grid test rotor flow computation run with $\Omega_{op} = 1.75$, $CFL_{op} = 2.80$. Standard values of fourth difference dissipation [12, 19], $\sigma_i = 0.03[|U_i| + c\sqrt{\nabla\xi_i \cdot \nabla\xi_i}]$, were used for this calculation, the local timesteps being computed from Eqs. (13) and (25). Due to the parabolic stability constraints arising from physical dissipation, Ω_{op} had to be lowered substantially when artificial dissipation was not incorporated in Eq. (25). The three dashed curves in Fig. 9 illustrate this. A choice of $\Omega_{op} = 0.6$ yielded a divergent solution; $\Omega_{op} = 0.5$ showed some unstable behavior in early stages of iteration (compare Fig. 8), but converged. $\Omega_{op} = 0.4$ provided a stable iterative process with a slightly diminished convergence rate. This demonstrates that it is useful to incorporate artificial dissipation in the parabolic timestep prescription in problems of this type, to avoid ad hoc specification of an optimum VonNeumann number which varies with the amount of artificial dissipation used.

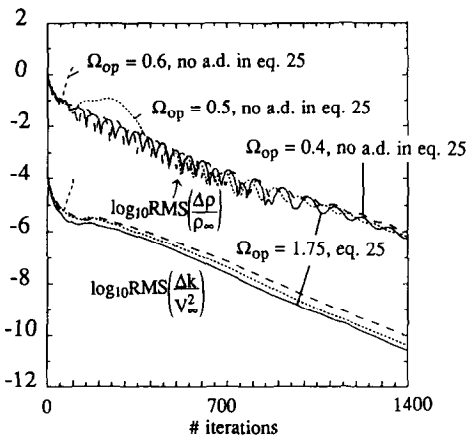

FIG. 9. Comparison of convergence rates for several operating VonNeumann numbers with (solid) and without (dashed) inclusion of artificial dissipation terms in timestep computations.

Algebraic Reynolds Stress Modelling (ARSM)

A class of algebraic Reynolds Stress models [30–32] can be cast in terms of an algebraic expression for the six individual Reynolds stress components,

$$-\overline{\rho u_i'' u_j''} = -\tfrac{2}{3}\delta_{ij}\rho k - \rho k T_{ij}, \tag{36}$$

where

$$T_{ij} = \frac{R_{ij}(2-C_2)/2 + (P_{ij} - 2P\,\delta_{ij}/3)(1-C_2)}{P + \rho\varepsilon(C_1 - 1)},$$

$$R_{ik} = -2\omega_p(\varepsilon_{ipj}\overline{\rho u_k'' u_j''} + \varepsilon_{kpj}\overline{\rho u_i'' u_j''})$$

$$P_{ij} = \left(-\overline{\rho u_i'' u_k''}\frac{\partial u_j}{\partial x_k} - \overline{\rho u_j'' u_k''}\frac{\partial u_i}{\partial x_k}\right), \qquad 2P = P_{ii}.$$

The effective stress tensors, for the $(k-\varepsilon)$ + ARSM are

$$\tau_{ij} = \mu_l\left[\left(\frac{\partial u_i}{\partial x_j} + \frac{\partial u_j}{\partial x_i}\right) - \frac{2}{3}\delta_{ij}\frac{\partial u_k}{\partial x_k}\right] + \mu_t\left[\left(\frac{\partial u_i}{\partial x_j} + \frac{\partial u_j}{\partial x_i}\right) - \frac{2}{3}\delta_{ij}\frac{\partial u_k}{\partial x_k}\right] - \frac{2}{3}\delta_{ij}\rho k \tag{37a}$$

$$\tau_{ij} = \mu_l\left[\left(\frac{\partial u_i}{\partial x_j} + \frac{\partial u_j}{\partial x_i}\right) - \frac{2}{3}\delta_{ij}\frac{\partial u_k}{\partial x_k}\right] - \rho k T_{ij} - \tfrac{2}{3}\delta_{ij}\rho k. \tag{37b}$$

So for the ARSM, an "anisotropic eddy viscosity" can be identified:

$$\mu_{tij} = -\rho k T_{ij} \Big/ \left[\left(\frac{\partial u_i}{\partial x_j} + \frac{\partial u_j}{\partial x_i}\right) - \frac{2}{3}\delta_{ij}\frac{\partial u_k}{\partial x_k}\right]. \tag{38}$$

In the present work, the high-Reynolds number ARSM due to Galmes and Lakshminarayana [30] was extended to treat regions where viscous damping effects become important (details in Kunz [13]). This model retains the same form as given in Eq. (36) and is consistent with the low-Reynolds number model used to provide values of k and ε. In the numerical implementation of the ARSM, the k and ε equations are not modified; however, the viscous fluxes in the momentum and energy equations incorporate the

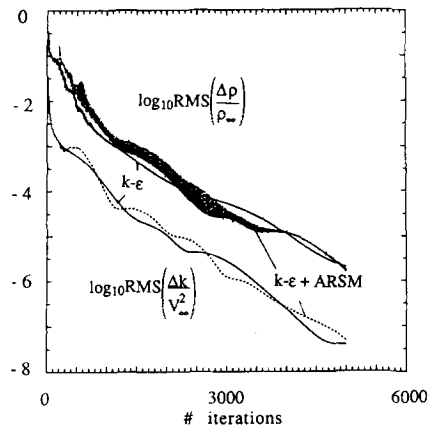

FIG. 10. Comparison of convergence rates for turbulent flat plate flow computation using $k-\varepsilon$ model (solid) and $k-\varepsilon$ + ARSM model (dashed). Spike in density residual at iteration 200 corresponds to when ARSM is first implemented.

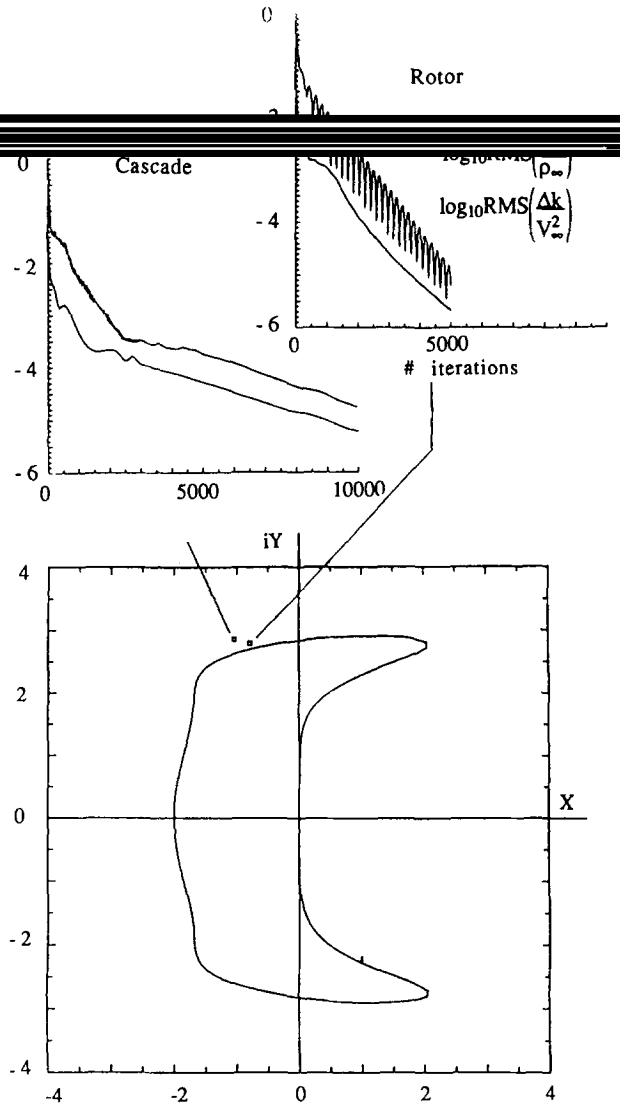

FIG. 11. Location of numerical operating point, (CFL_{op}, Ω_{op}), for full-scale cascade and rotor flow computations, plotted in the complex Z plane with the stability boundary for the RK4 scheme used. Corresponding convergence histories for these two calculations are also included.

effective stress as give in Eq. (37b). If it is assumed that the effective diffusivities provided by the two models are of the same order of magnitude, $\mu_{tij} = O(\mu_t)$, then the stability arguments provided in the previous sections remain valid when the ARSM is used. To illustrate this, a flat plate turbulent flow computation was performed using the two models. In Fig. 10, the convergence histories for the two models are plotted. It is seen that the convergence rates compare nearly identically.

Stability Boundary

The investigations reported earlier in this section, suggest that the rotation and turbulence source terms can be neglected in Eqs. (13) and (25), but all other terms including artificial dissipation should be included, and the procedures summarized in Eqs. (35a)–(35c) should be adopted. This gives rise to a robust and convergent code for computation of internal flows, including turbomachinery flows, using a low-Reynolds number $k-\varepsilon$ model in a fully explicit solution procedure. In Fig. 11, the location of CFL_{op} and Ω_{op} corresponding to maximum attainable convergence rates, for the *fine* grid cascade and rotor flow computations, are plotted with the stability boundary for the scheme. The locations of these operating points are very close to the scalar bound for the scheme (compare Fig. 1). The corresponding convergence histories for these two "production" runs also appear there. This figure provides additional support to the validity of the foregoing analyses in application to full scale engineering computations.

5. CONCLUSION

The conclusions of the present work can be summarized as follows:

(1) When applied to compressible internal flow computations, at convergence, the source terms in the k and ε equations do not significantly affect the local stability of explicit multistage schemes away from solid boundaries, and in the case of Chien's model, near such boundaries either.

(2) In early stages of iteration, terms proportional to $P/\rho\varepsilon$ and ε/k may be of some difficulty. For Chien's model, several ad hoc procedures, outlined in Eqs. (35a)–(35c) circumvent these problems. It was observed, that the ε/k term which appears in the stability analysis, may be responsible for near-wall instabilities in other low-Reynolds number models which solve a transport equation for the actual dissipation rate rather than its isotropic component.

(3) Consistent with the above conclusions, implicit treatment of the turbulence transport source terms is not necessary in the types of computations investigated, when Chien's model is used.

The authors believe that conclusions 1–3 are probably valid for some other low-Reynolds number models.

(4) Incorporation of an algebraic Reynolds stress model does not adversely affect the stability of the procedure.

(5) Including physical and artificial dissipation terms in the determination of local timesteps is crucial and desirable, respectively, for the engineering computation of turbomachinery flowfields when a two-equation turbulence model is used.

(6) System rotation has a negligible effect on the stability of these schemes for rotation numbers and meshes typical of viscous turbomachinery computations.

(7) Numerically coupling the discrete turbulence model to the mean flow equations has virtually no effect on the convergence, accuracy, and CPU performance of the scheme, so the analyst should decide whether to use a coupled or an uncoupled approach solely on the basis of practical considerations.

APPENDIX A

Conservative Primary Variable, Flux, and Source Vectors

$$\hat{Q}=\frac{1}{J}\begin{pmatrix}\rho\\ \rho u\\ \rho v\\ \rho w\\ \rho e_{OR}\\ \rho k\\ \rho\varepsilon\end{pmatrix},\quad \hat{S}=\frac{1}{J}\begin{pmatrix}0\\ 0\\ \rho(\omega^2 y+2\omega w)\\ \rho(\omega^2 z-2\omega v)\\ 0\\ P-\rho\varepsilon+\mathscr{D}\\ (C_1 f_1 P-C_2 f_2\rho\varepsilon)(\varepsilon/k)+\mathscr{E}\end{pmatrix},\quad \hat{E}=\frac{1}{J}\begin{pmatrix}\rho U\\ \rho uU+\xi_x p\\ \rho vU+\xi_y p\\ \rho wU+\xi_z p\\ (\rho e_{OR}+p)U\\ \rho kU\\ \rho\varepsilon U\end{pmatrix},\quad \hat{F}=\frac{1}{J}\begin{pmatrix}\rho V\\ \rho uV+\eta_x p\\ \rho vV+\eta_y p\\ \rho wV+\eta_z p\\ (\rho e_{OR}+p)V\\ \rho kV\\ \rho\varepsilon V\end{pmatrix},\quad \hat{G}=\frac{1}{J}\begin{pmatrix}\rho W\\ \rho uW+\zeta_x p\\ \rho vW+\zeta_y p\\ \rho wW+\zeta_z p\\ (\rho e_{OR}+p)W\\ \rho kW\\ \rho\varepsilon W\end{pmatrix},$$

Here u, v, w are cartesian velocities; U, V, W are contravariant velocities; ω is the angular velocity; ρ is the density; p is the static pressure; T is the static temperature, $e_{OR} = e' + (u^2+v^2+w^2)/2 - \omega^2 r^2/2$ is the total energy variable; k, ε are turbulent kinetic energy and dissipation rate; P is the turbulent kinetic energy production rate; $J, \xi_i, \eta_i, \zeta_i$ are the metric Jacobian and grid metrics; K, μ are diffusion coefficients; $C_1, C_2, \mathscr{D}, \mathscr{E}$ are turbulence modelling parameters.

$$\hat{E}_v = \frac{E_v\xi_x + F_v\xi_y + G_v\xi_z}{J}$$

$$= \frac{1}{J}\begin{bmatrix} 0 \\ \xi_x\tfrac{2}{3}\mu_e(2[u_\xi\xi_x + u_\eta\eta_x + u_\zeta\zeta_x] - [v_\xi\xi_y + v_\eta\eta_y + v_\zeta\zeta_y] - [w_\xi\xi_z + w_\eta\eta_z + w_\zeta\zeta_z]) + \xi_y\mu_e([u_\xi\xi_y + u_\eta\eta_y + u_\zeta\zeta_y] + [v_\xi\xi_x + v_\eta\eta_x + v_\zeta\zeta_x]) + \xi_z\mu_e([u_\xi\xi_z + u_\eta\eta_z + u_\zeta\zeta_z] + [w_\xi\xi_x + w_\eta\eta_x + w_\zeta\zeta_x]) - \xi_x\tfrac{2}{3}\rho k \\ \xi_x\mu_e([u_\xi\xi_y + u_\eta\eta_y + u_\zeta\zeta_y] + [v_\xi\xi_x + v_\eta\eta_x + v_\zeta\zeta_x]) + \xi_y\tfrac{2}{3}\mu_e(2[v_\xi\xi_y + v_\eta\eta_y + v_\zeta\zeta_y] - [u_\xi\xi_x + u_\eta\eta_x + u_\zeta\zeta_x] - [w_\xi\xi_z + w_\eta\eta_z + w_\zeta\zeta_z]) + \xi_z\mu_e([v_\xi\xi_z + v_\eta\eta_z + v_\zeta\zeta_z] + [w_\xi\xi_y + w_\eta\eta_y + w_\zeta\zeta_y]) - \xi_y\tfrac{2}{3}\rho k \\ \xi_x\mu_e([u_\xi\xi_z + u_\eta\eta_z + u_\zeta\zeta_z] + [w_\xi\xi_x + w_\eta\eta_x + w_\zeta\zeta_x]) + \xi_y\mu_e([v_\xi\xi_z + v_\eta\eta_z + v_\zeta\zeta_z] + [w_\xi\xi_y + w_\eta\eta_y + w_\zeta\zeta_y]) + \xi_z\tfrac{2}{3}\mu_e(2[w_\xi\xi_z + w_\eta\eta_z + w_\zeta\zeta_z] - [u_\xi\xi_x + u_\eta\eta_x + u_\zeta\zeta_x] - [v_\xi\xi_y + v_\eta\eta_y + v_\zeta\zeta_y]) - \xi_z\tfrac{2}{3}\rho k \\ \text{VISCOUS DEFORMATION WORK TERMS} + \xi_x k_e(T_\xi\xi_x + T_\eta\eta_x + T_\zeta\zeta_x) + \xi_y k_e(T_\xi\xi_y + T_\eta\eta_y + T_\zeta\zeta_y) + \xi_z k_e(T_\xi\xi_z + T_\eta\eta_z + T_\zeta\zeta_z) \\ \left(\mu_l + \frac{\mu_t}{\mathrm{Pr}_k}\right)\left[(\nabla\xi\cdot\nabla\xi)\frac{\partial k}{\partial\xi} + (\nabla\xi\cdot\nabla\eta)\frac{\partial k}{\partial\eta} + (\nabla\xi\cdot\nabla\zeta)\frac{\partial k}{\partial\zeta}\right] \\ \left(\mu_l + \frac{\mu_t}{\mathrm{Pr}_\varepsilon}\right)\left[(\nabla\xi\cdot\nabla\xi)\frac{\partial \varepsilon}{\partial\xi} + (\nabla\xi\cdot\nabla\eta)\frac{\partial \varepsilon}{\partial\eta} + (\nabla\xi\cdot\nabla\zeta)\frac{\partial \varepsilon}{\partial\zeta}\right] \end{bmatrix}$$

(with consistent expressions for $\hat{F}_v$ and $\hat{G}_v$).

Viscous Parameters

$$\tau_{ij}=\mu_e\left(\frac{\partial u_i}{\partial x_j}+\frac{\partial u_j}{\partial x_i}\right)-\frac{2}{3}\delta_{ij}\left(\mu_e\frac{\partial u_k}{\partial x_k}+\rho k\right),\quad q_i=-k_e\frac{\partial T}{\partial x_i}=\frac{k_e}{R}\left(\frac{p}{\rho^2}\right)\frac{\partial \rho}{\partial x_i}-\frac{k_e}{R}\left(\frac{1}{\rho}\right)\frac{\partial p}{\partial x_i},\quad \mu_e=\mu_l+\mu_t,$$

$$k_e=C_p\left(\frac{\mu_l}{\mathrm{Pr}_l}+\frac{\mu_t}{\mathrm{Pr}_t}\right),\quad P=\left[\mu_t\left(\frac{\partial u_i}{\partial x_j}+\frac{\partial u_j}{\partial x_i}\right)-\frac{2}{3}\delta_{ij}\left(\mu_t\frac{\partial u_k}{\partial x_k}+\rho k\right)\right]\frac{\partial u_j}{\partial x_i},\quad \mu_t=\frac{C_\mu \rho k^2}{\varepsilon}.$$

Modelling Parameters for Chien's Formulation

$$C_\mu=0.09*[1-\exp(-0.0115y^+)],\quad C_1=1.35,\quad f_1=1.00,\quad C_2=1.80,\quad f_2=[1-\tfrac{2}{9}\exp(-R_T^2/36)],$$

$$R_T=\frac{\rho k^2}{\mu_l\varepsilon},\quad y^+=\frac{\rho l u^*}{\mu_l},\quad u^*=\sqrt{\tau_w/\rho},\quad \mathscr{D}=-\frac{2\mu_l k}{l^2},\quad \mathscr{E}=-\frac{2\mu_l\varepsilon}{l^2}\exp(-0.5y^+),\quad \mathrm{Pr}_k=1.0,\quad \mathrm{Pr}_\varepsilon=1.3.$$

Here l is a wall proximity length scale; Pr_l, Pr_t are laminar and turbulent Prandtl numbers:

Nonconservative Jacobian Matrices

$$Q=\begin{pmatrix}\rho\\ u\\ v\\ w\\ p\\ k\\ \varepsilon\end{pmatrix},$$

$$\hat{A}_1=\begin{bmatrix}U & \rho\xi_x & \rho\xi_y & \rho\xi_z & 0 & 0 & 0\\ 0 & U & 0 & 0 & \frac{1}{\rho}\xi_x & 0 & 0\\ 0 & 0 & U & 0 & \frac{1}{\rho}\xi_y & 0 & 0\\ 0 & 0 & 0 & U & \frac{1}{\rho}\xi_z & 0 & 0\\ 0 & \xi_x\rho c^2 & \xi_y\rho c^2 & \xi_z\rho c^2 & U & 0 & 0\\ 0 & 0 & 0 & 0 & 0 & U & 0\\ 0 & 0 & 0 & 0 & 0 & 0 & U\end{bmatrix},\quad \hat{A}_2=\begin{bmatrix}V & \rho\eta_x & \rho\eta_y & \rho\eta_z & 0 & 0 & 0\\ 0 & V & 0 & 0 & \frac{1}{\rho}\eta_x & 0 & 0\\ 0 & 0 & V & 0 & \frac{1}{\rho}\eta_y & 0 & 0\\ 0 & 0 & 0 & V & \frac{1}{\rho}\eta_z & 0 & 0\\ 0 & \eta_x\rho c^2 & \eta_y\rho c^2 & \eta_z\rho c^2 & V & 0 & 0\\ 0 & 0 & 0 & 0 & 0 & V & 0\\ 0 & 0 & 0 & 0 & 0 & 0 & V\end{bmatrix},$$

$$\hat{A}_3=\begin{bmatrix}W & \rho\zeta_x & \rho\zeta_y & \zeta_z & 0 & 0 & 0\\ 0 & W & 0 & 0 & \frac{1}{\rho}\zeta_x & 0 & 0\\ 0 & 0 & W & 0 & \frac{1}{\rho}\zeta_y & 0 & 0\\ 0 & 0 & 0 & W & \frac{1}{\rho}\zeta_z & 0 & 0\\ 0 & \zeta_x\rho c^2 & \zeta_y\rho c^2 & \zeta_z\rho c^2 & W & 0 & 0\\ 0 & 0 & 0 & 0 & 0 & W & 0\\ 0 & 0 & 0 & 0 & 0 & 0 & W\end{bmatrix},\quad P=\begin{bmatrix}1 & 0 & 0 & 0 & 0 & 0 & 0\\ 0 & \frac{1}{\rho} & 0 & 0 & 0 & 0 & 0\\ 0 & 0 & \frac{1}{\rho} & 0 & 0 & 0 & 0\\ 0 & 0 & 0 & \frac{1}{\rho} & 0 & 0 & 0\\ 0 & 0 & 0 & 0 & \gamma-1 & 0 & 0\\ 0 & 0 & 0 & 0 & 0 & \frac{1}{\rho} & 0\\ 0 & 0 & 0 & 0 & 0 & 0 & \frac{1}{\rho}\end{bmatrix}$$

Here c is the speed of sound; γ is the specific heat ratio.

$$\hat{S}_1 = \begin{bmatrix} 0 & 0 & 0 & 0 & 0 & 0 & 0 \\ 0 & \frac{\mu_e}{\rho}\left(\nabla\xi\cdot\nabla\xi+\frac{1}{3}\xi_x\xi_x\right) & \frac{\mu_e}{\rho}\frac{1}{3}\xi_x\xi_y & \frac{\mu_e}{\rho}\frac{1}{3}\xi_x\xi_z & 0 & 0 & 0 \\ 0 & \frac{\mu_e}{\rho}\frac{1}{3}\xi_x\xi_y & \frac{\mu_e}{\rho}\left(\nabla\xi\cdot\nabla\xi+\frac{1}{3}\xi_y\xi_y\right) & \frac{\mu_e}{\rho}\frac{1}{3}\xi_y\xi_z & 0 & 0 & 0 \\ 0 & \frac{\mu_e}{\rho}\frac{1}{3}\xi_x\xi_z & \frac{\mu_e}{\rho}\frac{1}{3}\xi_y\xi_z & \frac{\mu_e}{\rho}\left(\nabla\xi\cdot\nabla\xi+\frac{1}{3}\xi_z\xi_z\right) & 0 & 0 & 0 \\ \gamma\left(\frac{\mu_l}{\mathrm{Pr}_l}+\frac{\mu_t}{\mathrm{Pr}_t}\right)\left(\frac{-p}{\rho^2}\right) & 0 & 0 & 0 & \gamma\left(\frac{\mu_l}{\mathrm{Pr}_l}+\frac{\mu_t}{\mathrm{Pr}_t}\right)\left(\frac{1}{\rho}\right) & 0 & 0 \\ \times(\nabla\xi\cdot\nabla\xi+\nabla\xi\cdot\nabla\eta+\nabla\xi\cdot\nabla\zeta) & & & & \times(\nabla\xi\cdot\nabla\xi+\nabla\xi\cdot\nabla\eta+\nabla\xi\cdot\nabla\zeta) & & \\ 0 & 0 & 0 & 0 & 0 & \frac{1}{\rho}\left(\mu_l+\frac{\mu_t}{\mathrm{Pr}_k}\right)(\nabla\xi\cdot\nabla\xi) & 0 \\ 0 & 0 & 0 & 0 & 0 & 0 & \frac{1}{\rho}\left(\mu_l+\frac{\mu_t}{\mathrm{Pr}_\varepsilon}\right)(\nabla\xi\cdot\nabla\xi) \end{bmatrix}$$

with consistent expressions for $\hat{S}_2$, $\hat{S}_3$.

$$\hat{T}_1 = \begin{bmatrix} 0 & 0 & 0 & 0 & 0 & 0 & 0 \\ 0 & \frac{2\mu_e}{\rho}\left(\nabla\xi\cdot\nabla\eta+\frac{1}{3}\xi_x\eta_x\right) & \frac{\mu_e}{\rho}\frac{1}{3}(\xi_x\eta_y+\xi_y\eta_x) & \frac{\mu_e}{\rho}\frac{1}{3}(\xi_x\eta_z+\xi_z\eta_x) & 0 & 0 & 0 \\ 0 & \frac{\mu_e}{\rho}\frac{1}{3}(\xi_x\eta_y+\xi_y\eta_x) & \frac{2\mu_e}{\rho}\left(\nabla\xi\cdot\nabla\eta+\frac{1}{3}\xi_y\eta_y\right) & \frac{\mu_e}{\rho}\frac{1}{3}(\xi_y\eta_z+\xi_z\eta_y) & 0 & 0 & 0 \\ 0 & \frac{\mu_e}{\rho}\frac{1}{3}(\xi_x\eta_z+\xi_z\eta_x) & \frac{\mu_e}{\rho}\frac{1}{3}(\xi_y\eta_z+\xi_z\eta_y) & \frac{2\mu_e}{\rho}\left(\nabla\xi\cdot\nabla\eta+\frac{1}{3}\xi_z\eta_z\right) & 0 & 0 & 0 \\ 0 & 0 & 0 & 0 & 0 & 0 & 0 \\ 0 & 0 & 0 & 0 & 0 & \frac{2}{\rho}\left(\mu_l+\frac{\mu_t}{\mathrm{Pr}_k}\right)(\nabla\xi\cdot\nabla\eta) & 0 \\ 0 & 0 & 0 & 0 & 0 & 0 & \frac{2}{\rho}\left(\mu_l+\frac{\mu_t}{\mathrm{Pr}_\varepsilon}\right)(\nabla\xi\cdot\nabla\eta) \end{bmatrix}$$

with consistent expressions for $\hat{T}_2$, $\hat{T}_3$.

$$\hat{D}_{\mathrm{I}} = \begin{bmatrix} 0 & 0 & 0 & 0 & 0 & 0 & 0 \\ 0 & 0 & 0 & 0 & 0 & 0 & 0 \\ 0 & 0 & 0 & 2\omega & 0 & 0 & 0 \\ 0 & 0 & -2\omega & 0 & 0 & 0 & 0 \\ 0 & 0 & 0 & 0 & 0 & 0 & 0 \\ 0 & 0 & 0 & 0 & 0 & 0 & -\left(\dfrac{P}{\rho\varepsilon}+1\right) \\ 0 & 0 & 0 & 0 & 0 & \left(C_1 f_1 \dfrac{P\varepsilon}{\rho k^2}+C_2 f_2 \dfrac{\varepsilon^2}{k^2}\right) & 0 \end{bmatrix},$$

$$\hat{D}_{\mathrm{R}} = \begin{bmatrix} 0 & 0 & 0 & 0 & 0 & 0 & 0 \\ 0 & 0 & 0 & 0 & 0 & 0 & 0 \\ 0 & 0 & 0 & 0 & 0 & 0 & 0 \\ 0 & 0 & 0 & 0 & 0 & 0 & 0 \\ 0 & 0 & 0 & 0 & 0 & 0 & 0 \\ 0 & 0 & 0 & 0 & 0 & \dfrac{2P}{\rho k}-\dfrac{2\mu_l}{\rho l^2} & 0 \\ 0 & 0 & 0 & 0 & 0 & 0 & \dfrac{-2C_2 f_2 \varepsilon}{k}-\dfrac{2\mu_l}{\rho l^2} e^{-y^+/2} \end{bmatrix}.$$

Fourier Matrix for Hyperbolic Stability

$$Z_1 = i \begin{bmatrix} US_\xi+VS_\eta+WS_\zeta & \rho(\xi_x S_\xi+\eta_x S_\eta+\zeta_x S_\zeta) & \rho(\xi_y S_\xi+\eta_y S_\eta+\zeta_y S_\zeta) & \rho(\xi_z S_\xi+\eta_z S_\eta+\zeta_z S_\zeta) & 0 & 0 & 0 \\ 0 & US_\xi+VS_\eta+WS_\zeta & 0 & 0 & \frac{1}{\rho}(\xi_x S_\xi+\eta_x S_\eta+\zeta_x S_\zeta) & 0 & 0 \\ 0 & 0 & US_\xi+VS_\eta+WS_\zeta & -2i\omega & \frac{1}{\rho}(\xi_y S_\xi+\eta_y S_\eta+\zeta_y S_\zeta) & 0 & 0 \\ 0 & 0 & 2i\omega & US_\xi+VS_\eta+WS_\zeta & \frac{1}{\rho}(\xi_z S_\xi+\eta_z S_\eta+\zeta_z S_\zeta) & 0 & 0 \\ 0 & \rho c^2(\xi_x S_\xi+\eta_x S_\eta+\zeta_x S_\zeta) & \rho c^2(\xi_y S_\xi+\eta_y S_\eta+\zeta_y S_\zeta) & \rho c^2(\xi_z S_\xi+\eta_z S_\eta+\zeta_z S_\zeta) & US_\xi+VS_\eta+WS_\zeta & 0 & 0 \\ 0 & 0 & 0 & 0 & 0 & US_\xi+VS_\eta+WS_\zeta & i\left(\frac{P}{\rho\varepsilon}+1\right) \\ 0 & 0 & 0 & 0 & 0 & -i\left(C_1 f_1 \frac{P\varepsilon}{\rho k^2}+C_2 f_2 \frac{\varepsilon^2}{k^2}\right) & US_\xi+VS_\eta+WS_\zeta \end{bmatrix}$$

ACKNOWLEDGMENTS

The first author was supported by a U.S. Army Research Office fellowship, through Grant DAAL03-86-G-0044, monitored by Dr. T. L. Doligalski. In addition, the following individuals were helpful in providing assistance and suggestions in the course of carrying out this work: S. Connell, G. Dulikravich, K. Kirtley, C. Merkle, P. Morris, and C. Olling. The authors wish to acknowledge the National Science Foundation supported Pittsburgh Supercomputer Center (Grants MSM860009P and CBT90015P) as well as the National Aerodynamic Simulation facility at NASA Ames Research Center for providing computer resources.

REFERENCES

1. B. Lakshminarayana, *AIAA J.* **24**, 1900 (1986).
2. T. J. Coakley, "Turbulence Modelling Methods for the Compressible Navier–Stokes Equations," AIAA Paper 83-1693, 1983 (unpublished).
3. P. Eliasson, Flygtekniska Forsoksanstalten TN 1988-19, Stockholm, 1988 (unpublished).
4. F. Grasso and C. G. Speziale, "Supersonic Flow Computations by Two-Equation Turbulence Modelling," AIAA Paper 89-1951, 1989 (unpublished).
5. D. G. Holmes and S. D. Connell, "Solution of the 2D Navier–Stokes Equations on Unstructured Adaptive Grids," AIAA Paper 89-1932, 1989 (unpublished).
6. J. S. Liu, Ph.D. thesis, MAE, Case Western Reserve University, 1987 (unpublished).
7. J. Sahu and J. Danberg, *AIAA J.* **24**, 1744 (1986).
8. F. Martelli and V. Michelassi, in *Recent Advances and Applications in Computational Fluid Dynamics*, edited by O. Baysal (ASME, New York, 1990).
9. G. A. Gerolymos, *AIAA J.* **28**, 1707 (1990).
10. D. Choi and C. J. Knight, "Computations of 3D Viscous Flows in Rotating Turbomachinery Blades," AIAA Paper 89-0323, 1989 (unpublished).
11. R. F. Kunz and B. Lakshminarayana, *AIAA J.* **30**, 13 (1992).
12. R. F. Kunz and B. Lakshminarayana, "Three-Dimensional Navier–Stokes Computation of Turbomachinery Flows Using an Explicit Numerical Procedure and a Coupled $k-\varepsilon$ Turbulence Model," *ASME J. Turbomachinery* **114**, 627 (1991).
13. R. F. Kunz, Ph.D. thesis, Department of Aerospace Engineering, Pennsylvania State University, 1991 (unpublished).
14. A. Jameson, W. Schmidt, and E. Turkel, "Numerical Solutions of the Euler equations by Finite Volume Methods Using Runge–Kutta Time-Stepping Schemes," AIAA Paper 81-1259, 1981 (unpublished).
15. S. Lee and G. Dulikravich, "Magnetohydrodynamic Flow Computations in Three Dimensions," AIAA Paper 91-0388, 1991 (unpublished).
16. R. W. Maccormack and B. S. Baldwin, "A Numerical Method for Solving the Navier–Stokes Equations with Application to Shock-Boundary Layer Interactions," AIAA Paper 75-4, 1975 (unpublished).
17. K. Chien, *AIAA J.* **20**, 33 (1982).
18. S. Abarbanel and D. Gottlieb, *J. Comput. Phys.* **41**, 1 (1981).
19. L. Martinelli, Ph.D. Thesis, MAE Department, Princeton University, 1987 (unpublished).
20. R. F. Warming, R. M. Beam, and B. J. Hyett, *Math. Comput.* **29**, 1037 (1975).
21. R. S. Varga, *Matrix Iterative Analysis* (Prentice–Hall, Englewood Cliffs, NJ, 1962).
22. G. W. Stewart, *Introduction to Matrix Computations* (Academic Press, New York/London, 1973).
23. J. O. Hinze, *Turbulence* (McGraw–Hill, New York, 1975).
24. C. K. G. Lam and K. A. Bremhorst, *J. Fluids Eng.* **103**, 460 (1981).
25. C. R. Olling, personal communication (1989).
26. K. Kirtley, personal communication (1989).
27. V. C. Patel, W. Rodi, and G. Scheuerer, *AIAA J.* **23**, 1308 (1985).
28. S. D. Connell, personal communications (1989–1990).
29. B. E. Launder and B. I. Sharma, *Lett. Heat Mass Transfer* **1**, 131 (1974).
30. J. M. Galmes and B. Lakshminarayana, *AIAA J.* **22**, 1420 (1984).
31. W. Rodi, *Z. Angew. Math. Mech.* **56**, T219 (1976).
32. H. I. Andersson and P. J. Nilsen, Report 89:01, The Norwegian Institue of Technology, Div. of Applied Mechanics, 1989 (unpublished).
33. D. J. Mavriplis and L. Martinelli, "Multigrid Solution of Compressible Turbulent Flow on Unstructured Meshes Using a Two-Equation Model," AIAA Paper 91-0237, 1991 (unpublished).